Author Contributions:

Conceptualization: S. S. Rao
Data curation: S. S. Rao
Formal analysis: S. S. Rao, Monti Chakraborty, Sandeep Kumar
Investigation: S. S. Rao
Methodology: S. S. Rao, Monti Chakraborty
Project Administration: Nandita Srivastava
Resources: S. S. Rao
Software: S. S. Rao, Monti Chakraborty, Sandeep Kumar

Observations of Geomagnetic Crochet at High-Latitudes Due To X1.5 Class Solar Flare on 3 July 2021

S. S. Rao[1] , **Nandita Srivastava[1]** , **Monti Chakraborty[2]** , **Sandeep Kumar[1,3]** , and **D. Chakrabarty[4]**

[1]Udaipur Solar Observatory, Physical Research Laboratory, Udaipur, India, [2]Departmentof Electronics and Communication Engineering, Tripura University, Agartala, India, [3]Discipline of Physics, Indian Institute of Technology Gandhinagar, Gandhinagar, Gujarat, India, [4]Space and Atmospheric Sciences Division, Physical Research Laboratory Ahmedabad, Ahmedabad, India

Abstract On 3 July 2021, an X1.5 solar flare from the National Oceanic and Atmospheric Administration solar Active Region AR12838 (24°N, 88°W) occurred at 14:18 UT, peaked at 14:29 UT, and decayed at 14:34 UT. The study of this X1.5 solar flare is significant due to its unique geomagnetic crochet feature at high latitudes and its effective signature on Earth. The study examined X-rays, the extreme ultraviolet spectrum, ionospheric equivalent current (IEC), and geomagnetic field components. The study reveals a sudden increase in IEC during the X1.5 flare episode, forming a zonal current region and producing a geomagnetic crochet signature in geomagnetic field components at high latitudes (50°–80°N) along the 11°–26°E longitude sector during the flare peak time. All three geomagnetic field components show different sensitivity to the solar flare effect (sfe), and the amplitude and phase of the geomagnetic crochet across latitudes (for a given longitude) are consistent with the variations in the IEC. The present study is the first to appraise geomagnetic crochets of low magnitude (8–40 nT) and short duration (10–15 min) at high latitudes, particularly in the polar cusp region, during the X-class limb flare.

Plain Language Summary The X1.5 solar flare at 14:18 UT on 3 July 2021, occurred in a newly formed solar active region AR12838 (24°N, 88°W) on the sun. The current study analyses the solar flare effect (sfe) signature at high latitude induced by an X1.5 flare, and compares the results from previous paper of Yamauchi et al. (2020, https://doi.org/10.5194/angeo-38-1159-2020). However, while that paper reported geomagnetic crochet of high amplitude (200 nT) and long duration (~2 hr), the present work reports geomagnetic crochet of small amplitude (40 nT) and short duration (~15 min). The current study is unique regarding observations of geomagnetic crochet in the polar cusp region.

1. Introduction

The 11-year sunspot cycle breeds severe space weather events envisioned by solar flares, coronal mass ejections, geomagnetic storms, enriched radiation, and energetic particle flux. A link between the sunspots occurrence and the frequency of solar flares has been studied and reported (Fröhlich, 2009; Grodji et al., 2022). Solar flares are cataclysmic events that release wavelength spectrum ranging from radio to visible light, EUV, X-rays, gamma rays, and energetic particles over a few minutes to hours (Tsurutani et al., 2009). Soft X-ray (0.1–10 nm) and extreme ultraviolet (EUV; 10–121.6 nm) fluxes are increased over 10–30 min by factors of 10–100 and 2–10, respectively, during solar flare episodes. The increased soft X-ray and EUV flux during solar flares disrupts the thermosphere-ionosphere (TI) systems, interfering with ground and satellite communication (Qian et al., 2011). The increased level of EUV radiation from the solar flare is absorbed in the Earth's upper atmosphere, inducing its prompt heating and expansion, which results in a sudden drag and lowering of low-orbiting satellites (Schwenn, 2006; Thome & Wagner, 1971). Extreme X-ray emission induces absorption in the lower ionospheric D layer, resulting in the deterioration or complete absorption of high-frequency (HF) signals, a process known as short-wave fadeout (SWF) or the Dellinger effect (Dellinger, 1937), which has been studied using the ionosonde observations at different sectors of the globe during different solar flare events for example, (Barta et al., 2019; Sahai et al., 2007). The D-RAP2 model (https://www.ngdc.noaa.gov/stp/drap/data) revealed that the maximum HF absorption of 35 MHz occurred during the peak time of the X1.5 solar flare and that normal HF propagation was maintained after 1600 UT on 3 July 2021 over the Atlantic region (Rao & Chakraborty, 2022). The Digital Ionogram Database of the Global Ionosphere Radio Observatory (GIRO) also reveals the SWF event during the X1.5 solar flare over the Atlantic region.

Solar flares can produce geomagnetic signatures in the sunlit hemisphere in addition to electron density enhancements and their consequences for SWF. An extensive and quick variation in the ionospheric electron density is observed during the solar flare. The ionospheric conductivity (σ) depends enormously on the plasma density of the ionosphere, which increases during a solar flare (Rastogi et al., 1999; Thome & Wagner, 1971). The enhanced soft X-ray and EUV rapidly increase ionization in the D and E regions below 150 km during the day (Qian et al., 2010) and consequently the electric conductivity in the D region changes. The latest findings by Gopika et al. (2021) revealed that on 24 September 2011, X1.9 class solar flare increased the plasma density in the D and E regions by 880% and 383%, respectively. The lower ionospheric electric current system is altered by adhering to the fundamental ohm's equation ($J = [E + U \times B]$, where E = electric field, U = neutral wind, B = geomagnetic field (Pudovkin, 1974). This effect increases as background plasma convection increases (Nishida, 1968). The increased ionospheric current further induces geomagnetic variations on Earth (Curto et al., 2016). This effect is known as geomagnetic crochet (Dodson & Hedeman, 1958) or the solar flare effect, sfe (Curto et al., 1994).

During the solar quiet period, the E-region current system at middle and low latitudes is dominated by the solar-quiet (Sq) current system (Chulliat et al., 2016), arising from the ionospheric wind dynamo process for example, (Richmond & Maute, 2014). Curto et al. (1994) demonstrated that the sfe strengthens the Sq currents and changes the Sq current pattern. However, Richmond and Venkateswaran (1971) demonstrated that the locations of the sfe current foci are often separated from those of the Sq current system because the Sq currents primarily flow in the E region, while sfe currents may extend into the D region. Using geomagnetic data from the INTERMAGNET worldwide network of ground-based magnetometers, Dmitriev and Yeh (2008) studied sfe effects during the Bastille Day flare on 14 July 2000, and the Halloween Day flare on 28 October 2003. The connection of geomagnetic crochet with equatorial electrojet and details on initial studies concerning magnetic crochet could be found elsewhere (Rastogi et al., 2013). Yamauchi et al. (2020) studied the high-latitude current system during the X9.3 solar flare of 6 September 2017. They observed geomagnetic crochet signatures for 3 hr duration at stations in the latitude range 68°–77°N near local noon. Thus, the distinctive influence of solar flares is the intensification of the ionospheric electric currents, resulting in variations in the geomagnetic field (or sfe). The detailed documentation on sfe studies has been presented in Curto (2020) and references therein. The study of the flare time variation of the high-latitude geomagnetic field had not been attempted for nearly 40 years, despite significant progress in satellite and radar measurements, until the most recent research work by Yamauchi et al. (2020) of the solar flare event on 6 September 2017. They have distinguished between sub-solar and high-latitude crochet based amplitude and duration. Curto (2020) studied the same flare using the spherical elementary current system and presented sfe effects in the northward, eastward, and vertical components of geomagnetic fields over the magnetogram stations located at a low-mid latitude in the American and European-African sectors. Grodji et al. (2022) studied the sfe at magnetometer stations located globally in the latitude band 50°S–50°N during the solar flares of solar cycle-23 and -24. However, the magnetic crochet feature has extensively been studied at equatorial latitudes for example (Gopika et al., 2021; Rastogi et al., 1965, 1999), and references therein.

In this context, the current work is significant as we report geomagnetic crochet features at high-latitudes during the X-class solar flare. We report the effects of first X-class solar flare of solar cycle 25; it is a unique case of 3 July 2021 in which an unpredicted solar flare occurred from newly emerged sunspots group which was associated with the high-latitude geomagnetic crochet signatures in the latitudinal belt of 50°–80°N with some peculiar characteristics.

2. Observations

The Atmospheric Imaging Assembly (AIA) 211 Å (level 1) images, HMI continuum and HMI-LOS magnetogram images with 720 s cadence have been obtained from Joint Science Operations Center (JSOC) website at http://jsoc.stanford.edu/ajax/exportdata.html. The EUV Sensor (EUVS) and X-Ray Sensor (XRS) Irradiance Sensors (EXIS) on board the GOES-R satellites provide the XRS-A/B and EUV irradiance data (https://www.ncei.noaa.gov). In the present analysis, we used the 1-min averaged XRS-B (0.1–0.8 nm), and EUV irradiance for 25.6, 28.0, 29.0, 28.4, 30.0, and 31.0 nm for 3 July 2021 flare. The 1-min averaged geomagnetic field data of X (north), Y (east), and Z (vertical) components were obtained using the International Monitor for Auroral Geomagnetic Effects (IMAGE) magnetometer's interface, https://space.fmi.fi/image, and the INTERMAGNET magnetometer data were obtained from the url link: https://www.intermagnet.org/. The detail of magnetometer stations is given in Table 1. The instant-run interface at url https://space.fmi.fi/MIRACLE has been used to

Table 1
A List of Magnetometer Stations Included in the Present Study and Their Geographic Locations

IMAGE magnetometer stations	Geographic latitude	Geographic longitude
NAL	78.92°N	11.95°E
LYR	78.20°N	15.82°E
HOR	77.00°N	15.60°E
BJN	74.50°N	19.20°E
SOR	70.54°N	22.22°E
MAS	69.46°N	23.70°E
MUO	68.02°N	25.53°E
PEL	66.90°N	24.08°E
NUR	60.50°N	24.65°E
TAR	58.26°N	26.46°E
SUW	54.01°N	23.18°E
PPN	51.45°N	23.13°E
INTERMAGNET stations	Geographic latitude	Geographic longitude
HRN	77.00°N	15.54°E
ABK	68.35°N	18.82°E
UPS	59.90°N	17.35°E
DUR	41.35°N	14.46°E

obtain two-dimensional data of equivalent ionospheric current (IEC) vectors in a latitude-longitude grid. The Scandinavian ground magnetometer network IMAGE's magnetometer measurements, with a time resolution of 10 s, serve as the input data for calculating the ionospheric currents in the European Cluster Assimilation Technology (ECLAT) project.

3. Analysis and Results

3.1. Occurrence of X1.5 Solar Flare

The NOAA AR12838 appeared initially as a bipolar magnetic region on 2 July 2021, at 11:48 UT on the west limb, as shown in the attached movie (see Supporting Information@AR12838 Movie.MP4 (Movie S1) or available at https://drive.google.com/file/d/1KbPD-3RWQBFfSoZP2vHxb5bF5KlqyDpT/view?usp=drive_link). It was identified as β-type AR by NOAA, as shown in the middle panel of Figure 1. Although in HMI continuum images, these regions appeared as pores, as shown in the top panel of Figure 1. It was later classified as an AR by NOAA (https://www.solarmonitor.org/full_disk.php?date=20210704region12838&type=saia_00193&indexnum=1) when it produced X1.5 class flare at the time 14:18 UT whose intensity peaked at 14:29 UT on 3 July 2021. AR12838 produced the X1.5 flare at 14:18 UT within 13 hr of its first appearance in the HMI-LOS magnetogram. By this time, the magnetograms appear much more complicated because of the limb effects of magnetic field measurements, as shown in the movie. After the flare, the AR moved very close to the west limb of the Sun. The AR did not return in the next solar rotation. This shows that the total lifetime of NOAA AR12838 was less than half of the angular period of the sun, and thus it was a short-lived AR in Earth's frame of reference. It is well known that the large sunspot regions have a tendency to produce large flares (Watari, 2022). Further, the magnetic class of the AR is also associated with the occurrence of large flares, that is, ARs with more complex magnetic configurations produce larger flares (Sammis et al., 2000). Interestingly AR12838 was classified as β-type AR by NOAA. However, it gave rise to an X1.5 class flare. The top panel of Figure 2 shows sharp and prominent XRS B peaks at ~14:29 UT on July 3 corresponding to X1.5 solar flare, whose peak intensity increased to $1.5E-04$ W/m^2. The solar EUV irradiance changes significantly due to the transient solar flares, resulting in corresponding changes in the electron density, temperature, and composition of the thermosphere and ionosphere. Solar EUV (10–121 nm) irradiance is the direct energy input into the Earth's upper atmosphere at all
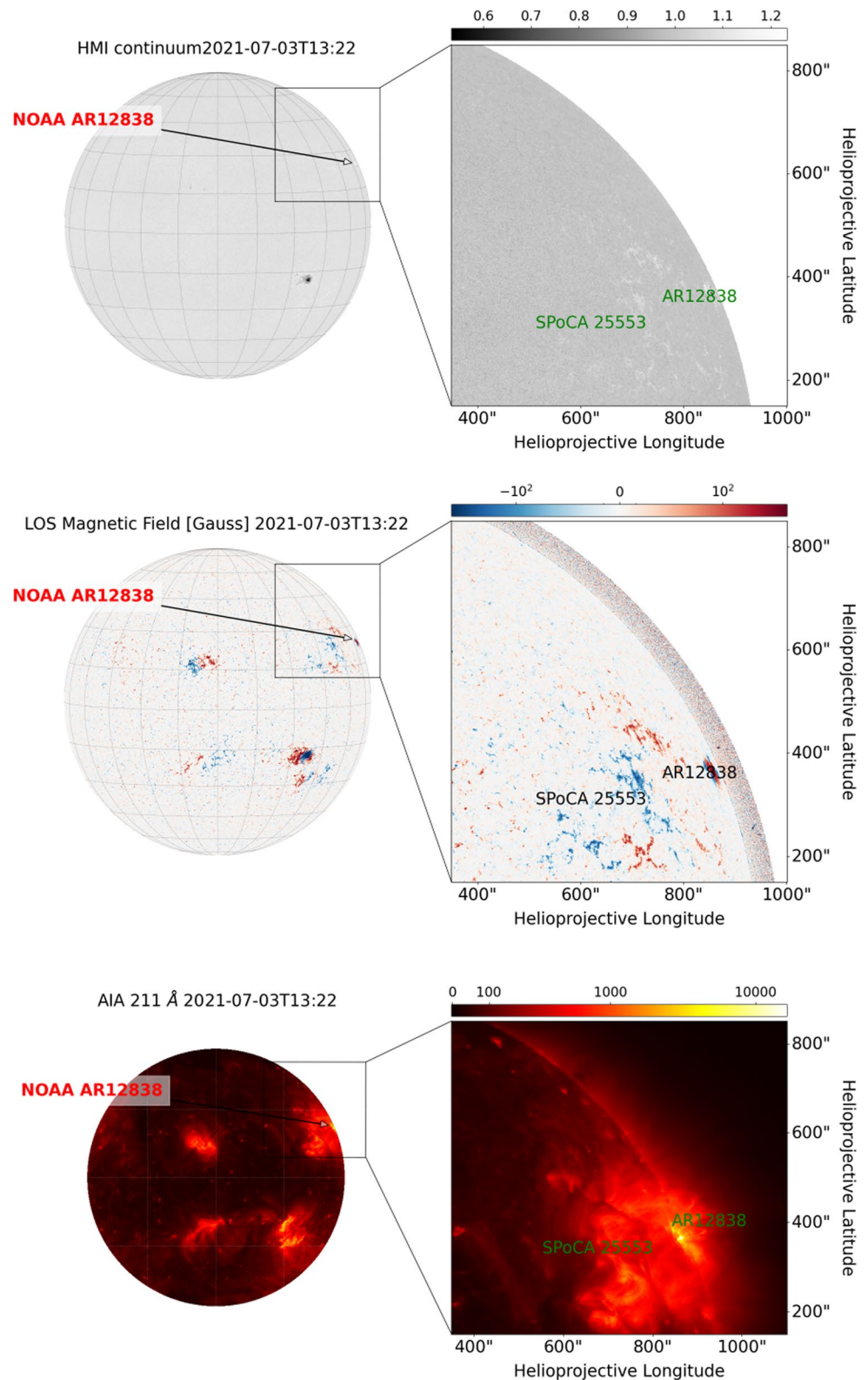
Figure 1. Top panel shows the location of the AR on the west limb in the HMI continuum image on 3 July 2021. The middle panel shows the HMI LOS magnetogram with newly emerging AR 12838. The bottom panel shows the AIA 211 Å images wherein other AR 25553 shown in the window is identified by the Spatial Possibilistic Clustering Algorithm (SPoCA).
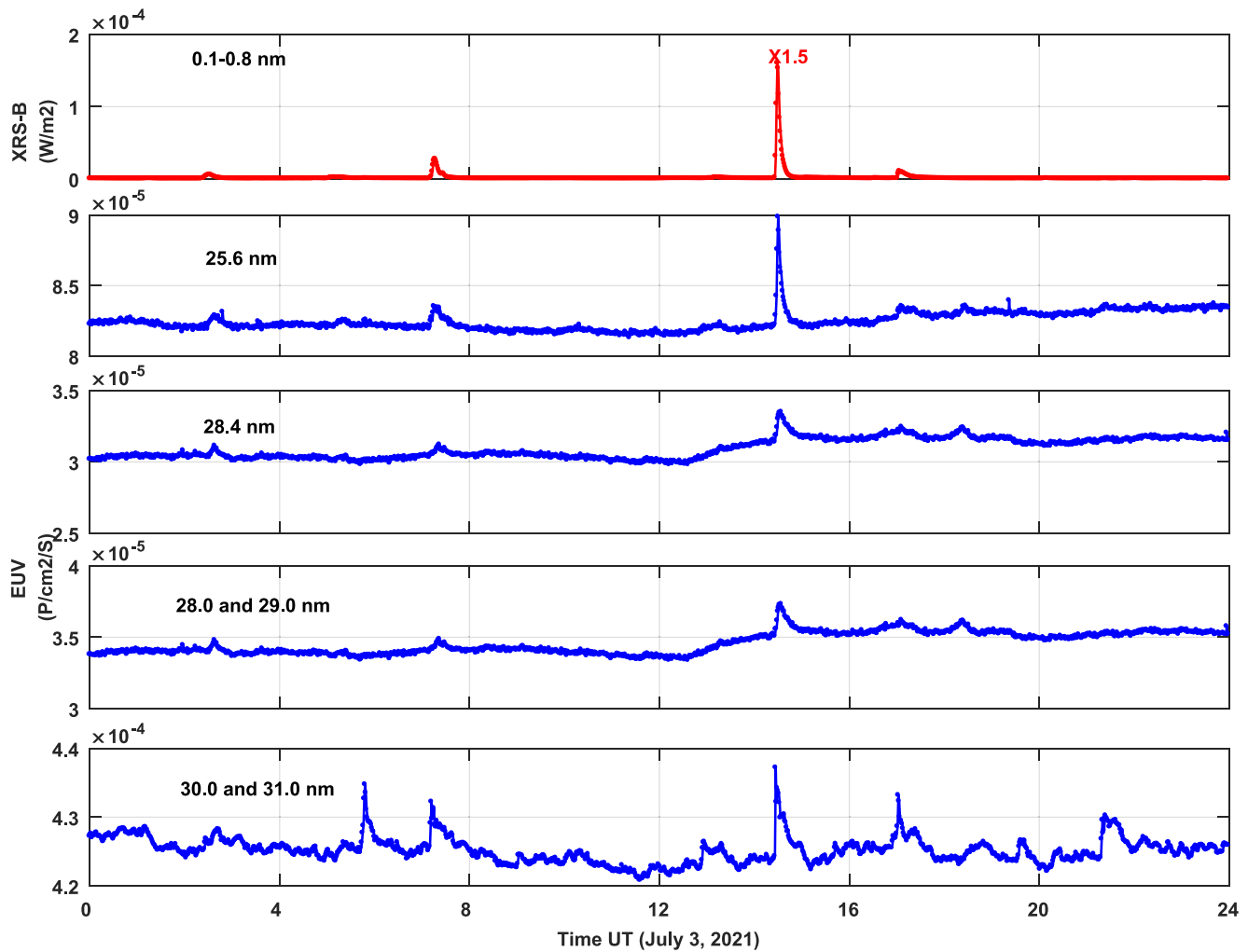
Figure 2. The upper panel gives the temporal variation variation of X-ray flux, XRS-B (0.1–0.8 nm) and lower panels shows the temporal variation of 1-min averages of EUV solar irradiances for 25.6, 28.0, 29.0, 28.4, 30.0, and 31.0 nm lines on 3 July 2021.

latitudes. Therefore, we have also plotted the variation of 1-min averaged EUV at different wavelength bands (lower panels of Figure 2), which shows distinct EUV flux peaks during the peak hour (14:29 UT) of the X1.5-class flare.

3.2. Geomagnetic Crochet Signatures of X1.5 Flare

The X1.5 flare event is not only special in terms of characteristics of source region but it is also a rare event wherein we observed geomagnetic crochet feature at geographic high-latitudes as consequences which is discussed hereafter. In order to study the solar flare-induced geomagnetic variations, the variation of the northern (X), eastern (Y), and vertical (Z) components of the geomagnetic field of chosen high-latitude magnetometer stations (shown in Table-1) in the longitudinal grid of 11°–26°E during the X1.5 solar flare of 3 July 2021, is presented. The results concerning geomagnetic variations are discussed in different sub-sections for different latitude belts.

3.2.1. Geomagnetic Observations in the Latitudinal Belt 74°–79°

The variation of 1-min averaged IMAGE magnetometer data of geomagnetic field components (X, Y, and Z) of the stations NAL (Geog. Lat. 78.92°N Geog. Long. 11.95°E), LYR (Geog. Lat. 78.20°N Geog. Long. 15.82°E), HOR (Geog. Lat. 77.00°N Geog. Long. 15.60°E), and BJN (Geog. Lat. 74.50°N Geog. Long. 19.20°E) located in the Svalbard high-latitude region is shown in Figure 3.
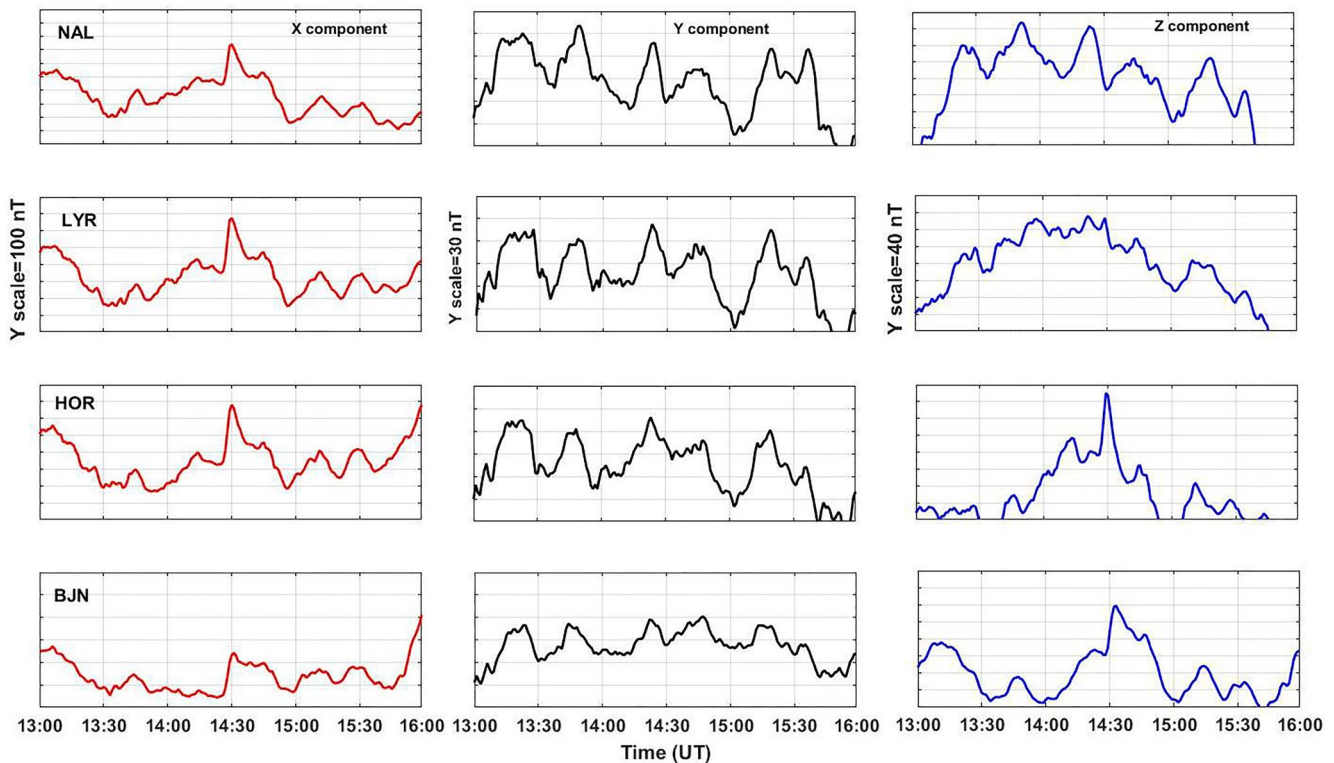
Figure 3. The variation of the 1-min averaged values of X, Y, and Z components of the geomagnetic field during the X1.5 solar flare are displayed at the high latitude stations NAL (78.92°N, 11.95°E), LYR (78.20°N, 15.82°E), HOR (77.00°N, 15.60°E), and BJN (74.50°N, 19.20°E).

An explicit hook-type positive spike in the X component of the geomagnetic field can be seen during the X1.5 solar flare peak time (14:29 UT) at several stations in the Svalbard's high-latitude region. The observed spike shape in the variation of geomagnetic field components induced by solar flare is typically known as geomagnetic crochet (Dodson & Hedeman, 1958). The X component spike persisted for 10–15 min, taking ~30 min to revert to normal fluctuation. The amplitude of the spike in the X component was ~40 nT at NAL, ~32 nT at LYR, ~28 nT at HOR, and ~8 nT at BJN suggested that the strength of the geomagnetic crochet decreased from poleward to equatorward stations. The observed latitudinal variation of crochet strength is related to the latitudinal distribution of the Ionospheric Equivalent Current (IEC), for which a detailed explanation is given in the discussion section. At the stations, LYR, HOR, HOP, and BJN, similar crochet structures of lesser magnitude can also be seen in the Z component of the geomagnetic field (right panel, Figure 3).

One can also note that the sudden and sharp spike (hook shape) in the X and Z components appeared simultaneously at stations LYR, HOR, and HOP but delayed by 4 min at BJN. The crochet shape is not distinct in the Y component (middle panel, Figure 3), which may have been masked by irregular geomagnetic variation as also noted by Grodji et al. (2022). The time sequence in the appearance of geomagnetic crochet is further explained in Section 4.4 of discussion section based on the time evolution of the ionospheric equivalent current, IEC (Figure 8). Thus, we have observed short-lived (10–15 min) and lower-amplitude (8–40 nT) crochet signatures at high-latitude (>75°N) in the Svalbard region. Yamauchi et al. (2020) observed broad maximum in variation of geomagnetic field component ΔX at stations LYB, HOP, BJN and in ΔH at stations DMH and DIK associated with X9.3 flare of 6 September 2017. Their observations showed a sharp increase in geomagnetic field magnitude from 65 to 130 nT within 15 min which was sustained at ~200 nT for an hour. Yamauchi et al. (2020) termed this crochet of broad maximum a "new high latitude crochet," which had a large amplitude (a maximum of ~200 nT) and longer duration (≥2 hr). In our case the analysis shows sudden and sharper spikes in X component of geomagnetic field with smaller amplitude (8–40 nT) and relatively shorter duration (~15 min). This could be clarified by comparing Figure 1 of Yamauchi et al. (2020) and Figure 3 in the current case. Stations in both the cases are located at roughly the same latitude belt (~74°–79°N). Thus it is clear that the Yamauchi et al. (2020)
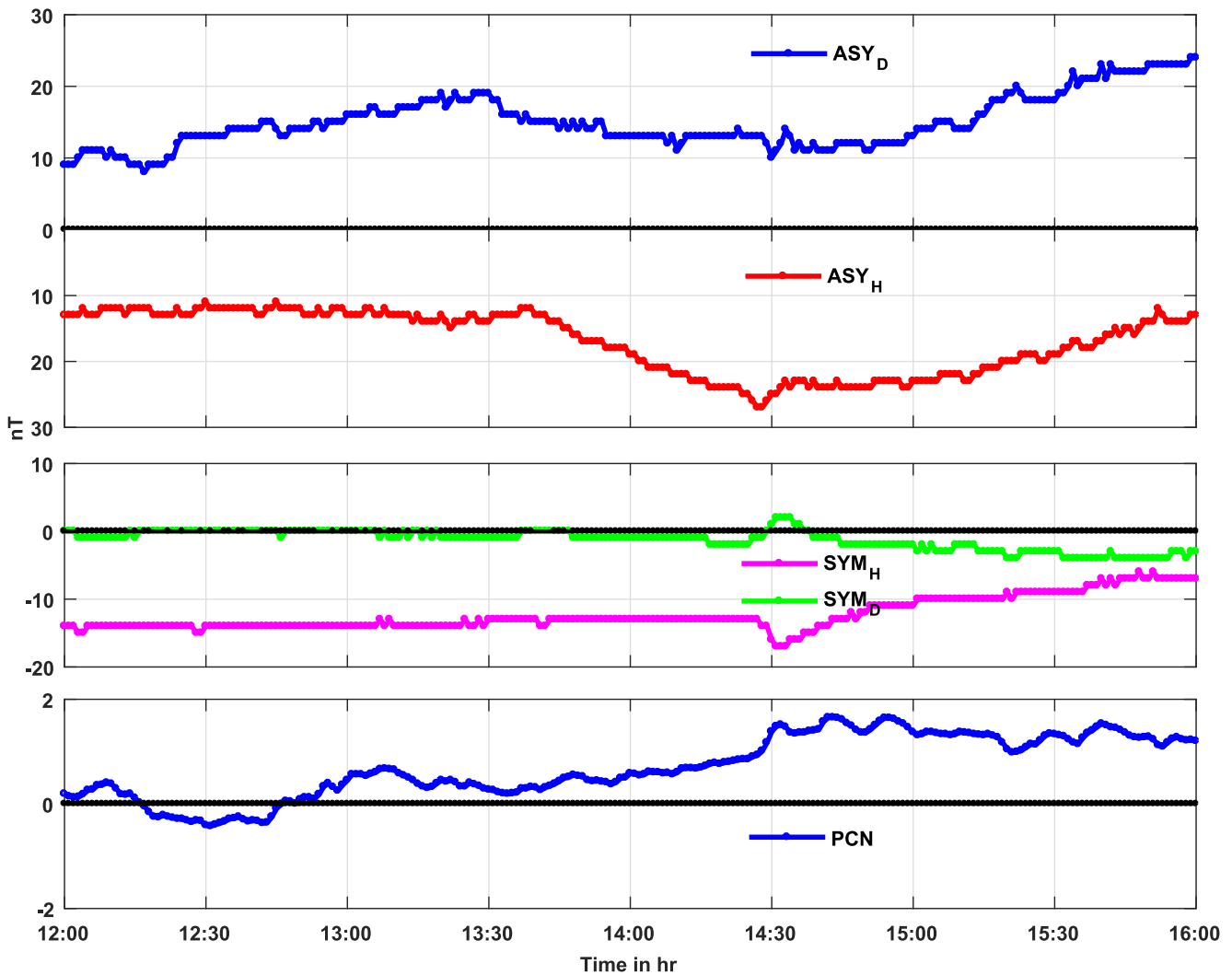
Figure 4. Variations of the ASY index, SYM index, and northern Polar Cap Electric field around the X1.5 solar flare of 3 July 2021 are shown.

did not observe spike feature at stations located >75°N. They observed only the broad maximum in ΔH variation at stations LYB, HOP, BJN DMH, and DIK. However, at BJN station, the broad maximum in geomagnetic field variation led to negative spike.

The latitudinal location of stations where geomagnetic crochet features are observed in the present case is close to and inside the invariant latitudinal location (∼77°N) of the polar cusp at noon, whose lower boundary may shift to 70° latitude during the post-noon hours (Russell, 2000). Thus, based on the location of observing stations and characteristics (duration and amplitude), the present observations of the geomagnetic signatures during the X1.5 class solar flare at the Svalbard region may be classified as a cusp-type geomagnetic crochet. Also, the present work is the first study wherein we report geomagnetic crochet at the polar cusp region (75°N–80°N). The effect can also be seen in the northern polar cap electric field (PCN) shown in Figure 4. The geomagnetic crochet shape can also be seen in the SYM-H and SYM-D indices at 14:29 UT (Figure 4). Additionally, the absence of crochet features in the ASY-H and ASY-D indices supports our conclusion that the geomagnetic disturbances detected in the Svalbard region are of the cusp type because the auroral and cusp crochets are not expected to contribute to ASY (Yamauchi et al., 2020). Other important contributors to the transient geomagnetic variations are solar energetic particles (SEP) and sub-storm activity in the cusp region at high latitudes. Hence, studying the sfe requires very accurate verification of the other sources of transient geomagnetic activity from magnetospheric origin. We have checked (not shown here) that the geomagnetic field was at quiet levels for a couple of weeks prior to
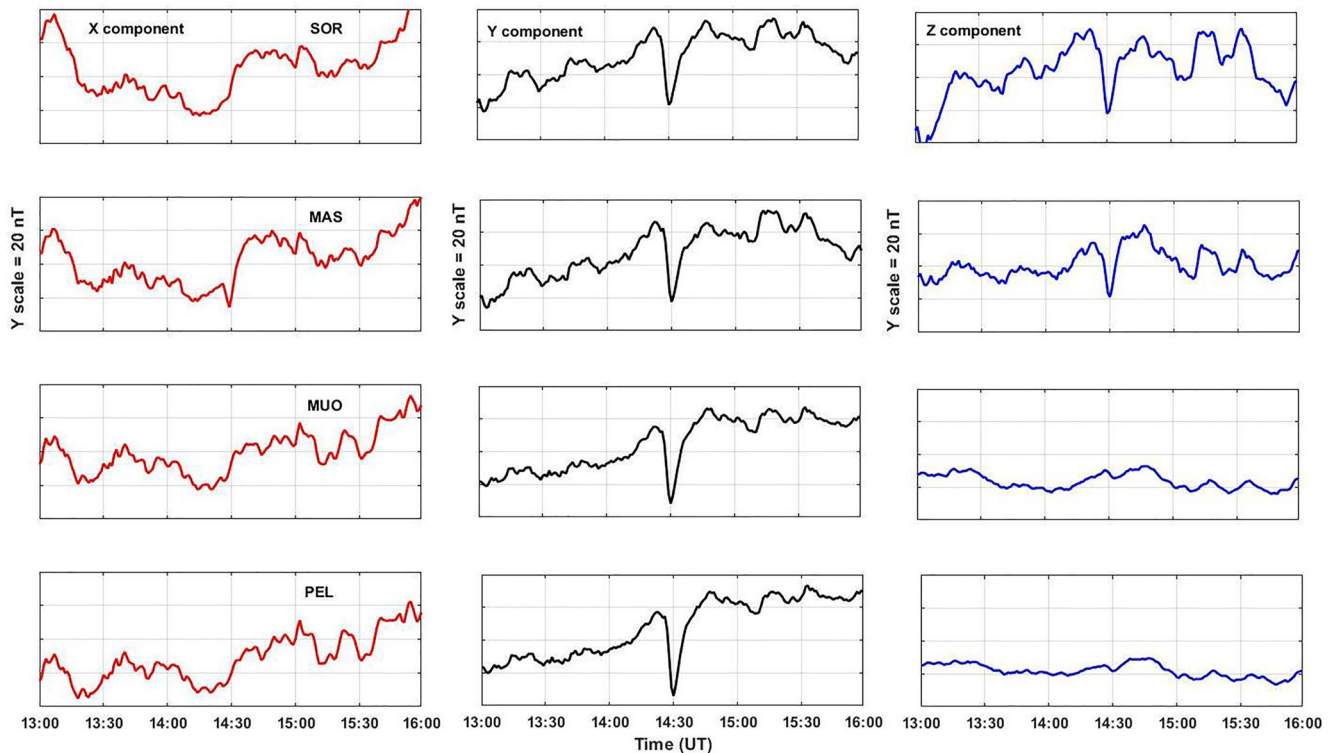
Figure 5. The variation of 1-min averaged values of X, Y, and Z components at station SOR (70.54N, 22.22E), MAS (69.46N, 23.70E), MUO (68.02N, 25.53E), and PEL (66.90N, 24.08E) are shown.

3 July 2021, and also that no Earth-directed CME occurred prior to 3 July 2021, whose geomagnetic signature could have coincided with the signatures of the X1.5 solar flare. The westward auroral electrojet (AL) variations (not shown here) reveal that there was no intensification of westward auroral electrojet current during flare time indicating absence of substorm. Hence, the geomagnetic variations observed in the polar cusp region are fully sfes and are not related to magnetospheric origin.

The observed geomagnetic disturbances are significant because the magnetosheath plasma directly accesses the ionosphere via the polar cusp (Newell & Meng, 1988; Willis, 1969). The most active manifestations of geomagnetic disturbances and geomagnetically induced currents (GICs) were observed at auroral latitudes and cusp regions. For example, the Finnish and Swedish power lines gained several amperes higher currents, and power lines had operational issues due to the GICs (Viljanen, 1997). Also, the cusp region is the most perturbed region for GNSS phase scintillation (Prikryl et al., 2011). Observing cusp geomagnetic crochets is particularly helpful for prediction since the geomagnetic disturbances of solar flare impacts are rapid and have vigorous signs at the cusp region.

3.2.2. Geomagnetic Observations in the Latitudinal Belt 66°–71°N

The variation of X, Y, and Z components at stations SOR (70.54°N, 22.22°E), MAS (69.46°N, 23.70°E), MUO (68.02°N, 25.53°E), and PEL (66.90°N, 24.08°E) is shown in Figure 5. The variation of X component reveals that no clear spike was recorded at any stations other than MAS, where a reversed spike in the X component (~5 nT) occurred around 14:30 UT. Although at around 14:30 UT, there was a rise in the X field of the order of ~5 nT with multiple fluctuations that persisted for more than 30 min at all stations. The Y component shows a negative spike of ~10 nT amplitude at all stations that lasted for 20 min, followed by a prolonged positive enhanced trailing phase of about 2 hr (middle panel, Figure 5). The order of positive enhanced level was ~5 nT. SOR and MAS stations exhibit a similar variation in the Z component with maximum amplitude of ~10 nT, whereas MUO and PEL exhibit a significantly weaker (~2 nT) and delayed (~2 min) negative crochet (right panel, Figure 5). The present observations of a negative spike in the geomagnetic field components at SOR, MAS, MUO, and PEL are

similar to "sub-solar type crochet" reported by Yamauchi et al. (2020) at stations SOR (70.5°N), TRO (69.7°N), KIR (67.8°N) and RVK(65.0°N) during the X9.3 flare of September 2017. However the amplitudes of negative spike were ~40 nT in case of Yamauchi et al. (2020) which is much longer than the 5–10 nT recorded in the present case. Furthermore, the amplitudes of post-spike enhanced level of ΔH at above mentioned stations in study of Yamauchi et al. (2020) were in range of 70–180 nT. In the present case, the amplitude of post spike enhanced level is recorded ~5 nT which is much lower than that in Yamauchi et al. (2020). Thus, the profile of post-spike enhanced level of the X and Y components in the present case of 3 July 2021 that was sustained for ~2 hr embodied multiple peaks seem analogous to the "newly defined high latitude crochet" by Yamauchi et al. (2020). However, the amplitude of the enhanced level of the geomagnetic field components during the recovery phase of X1.5 flare is much lower than that in Yamauchi et al. (2020).

3.2.3. Geomagnetic Observations in the Latitudinal Belt 50°–60°N

The variation of the X, Y, and Z components at the stations NUR (60.50°N, 24.65°E), TAR (58.26°N, 26.46°E), SUW (54.01°N, 23.18°E), and PPN (51.45°N, 23.13°E) is shown in Figure 6. The X field began to grow immediately after the flare peak time, reached its maximum magnitude ~5–8 nT, and stayed elevated for an hour. However, the typical crochet shape in the X component is only visible at TAR and SUW stations with maximum peak amplitude of ~5 nT.

The middle panel of Figure 6 shows a crochet shape in the Y component during the flare peak. The negative spike in the Y component at NUR, TAR, SUW, and PPN had an amplitude of ~10 nT and lasted for 10–15 min and coincided with the flare peak time. The negative spike settled at ~14:45 UT but did not attain the regular trend; instead, it continuously increased (up to 5–7 nT) for more than 2 hr. The Z component (right panel, Figure 6) also shows short lived crochet at 14:30 UT over all stations. However, the phase of the spike was positive at TAR and negative at the all other stations.
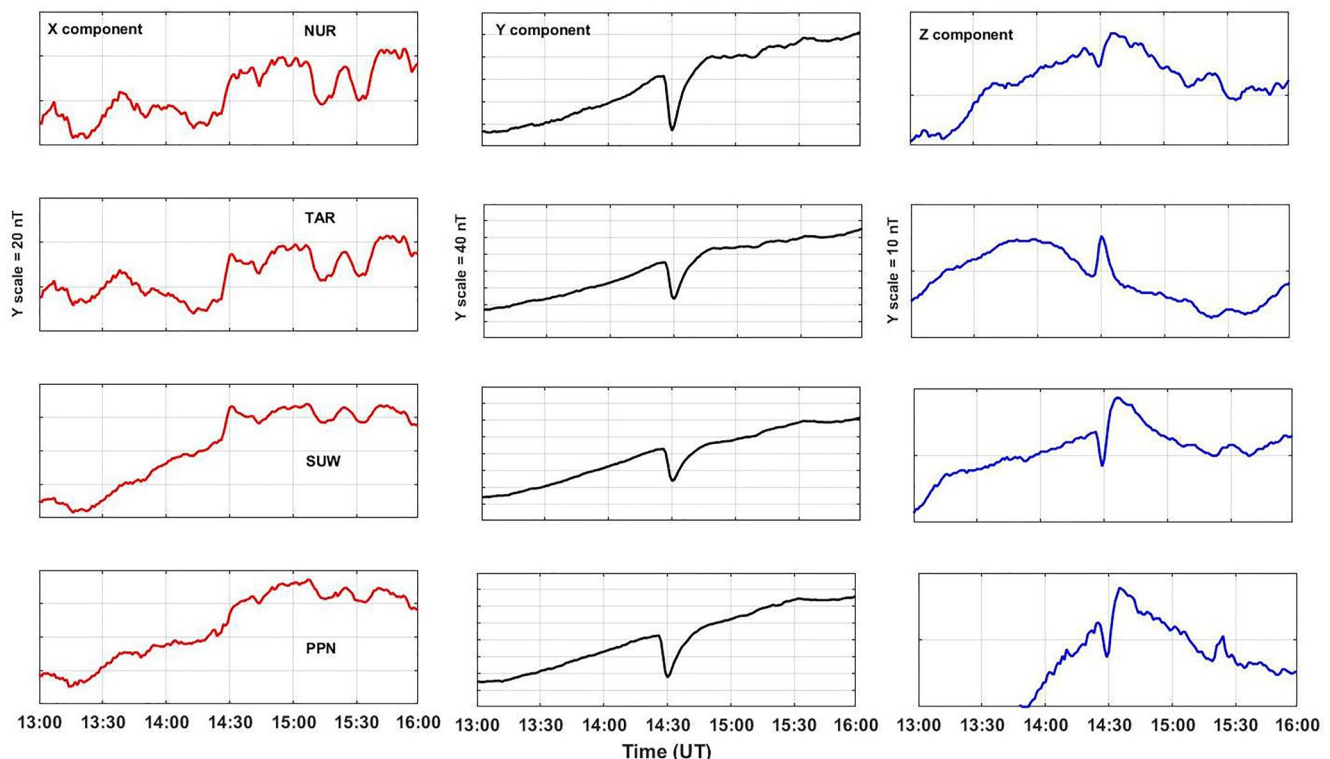

Figure 6. The variation of 1-min averaged values of X, Y, and Z components at station NUR (60.50°N, 24.65°E), TAR (58.26°N, 26.46°E), SUW (54.01°N, 23.18°E), and PPN (51.45°N, 23.13°E) are shown.

3.2.4. Geomagnetic Field Variations Over INTERMAGNET Magnetometer Stations

The IMAGE ground magnetometer results are also supported by the INTERMAGNET geomagnetic data (Figure 7). We have presented normalized values of X, Y, and Z components at stations HRN (77.00°N, 15.54°E), ABK (68.35°N, 18.82°E), UPS (59.90°N, 17.35°E), and DUR (41.35°N, 14.46°E). Similar to IMAGE magnetometer observations, the INTERMAGNET observations also do not show spike features in Y component during flare peak time at the HRN station. Also, a depletion (negative crochet) followed by increase in the opposite phase for an hour is observed at all INTERMAGNET stations. However, the normalized amplitude of X, Y, and Z disturbances remained small (±3 nT).
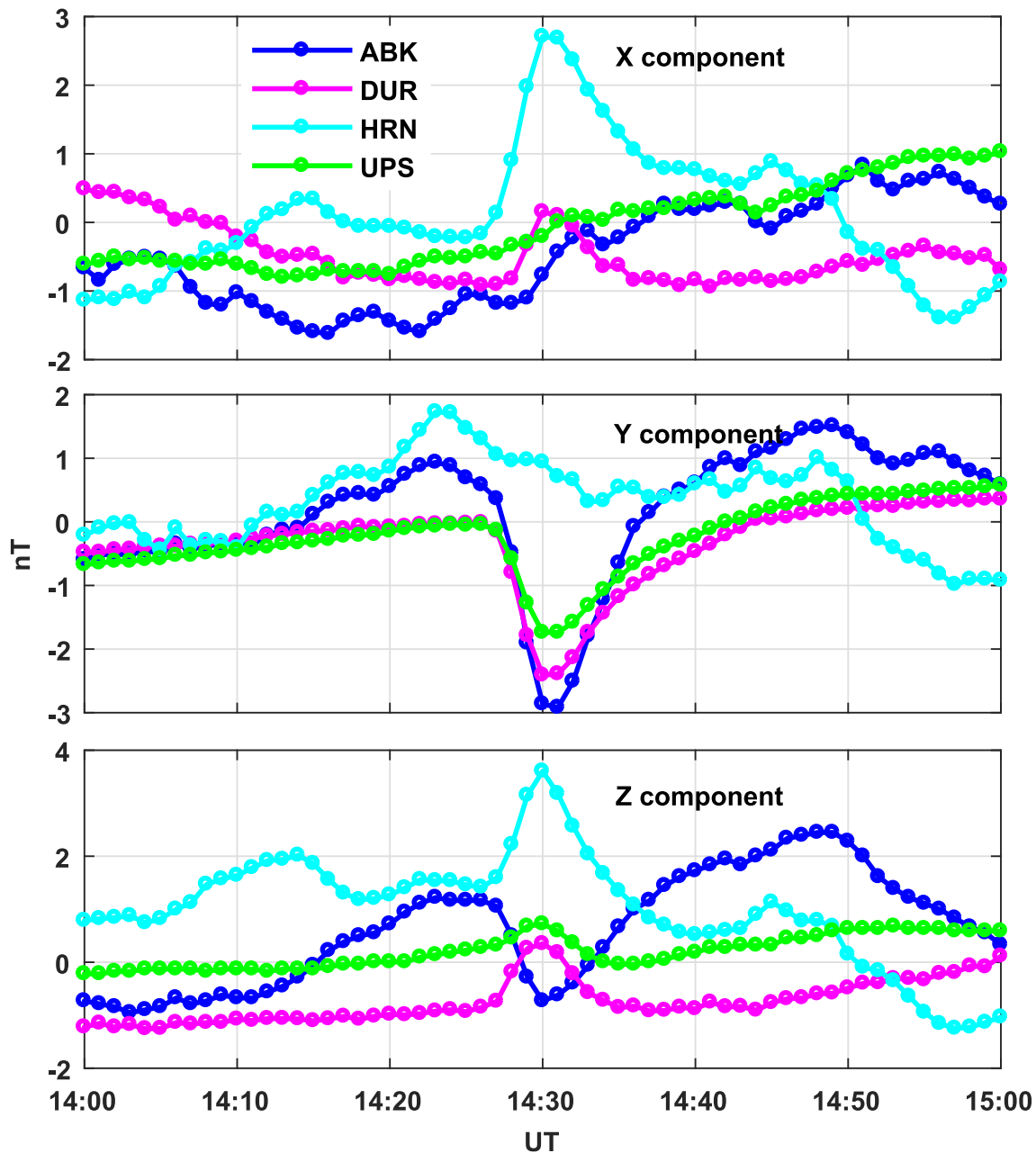

Figure 7. The variation of normalized values of X, Y, and Z components at stations HRN (77.00N, 15.54E), ABK (68.35N, 18.82E), UPS (59.90N, 17.35E), and DUR (41.35N, 14.46E) of Intermagnet network are shown.

4. Discussion

In the above section, we have presented the observation of the geomagnetic crochet signatures at the stations in the latitudinal belt of 50°–80°N along the ~11°–26°E longitudinal grid. Highly intriguing and significant observations have been made, and each one is discussed below.

4.1. Latitudinal Response of Sfe

Latitudinally, at first, the X component responded to flare-induced current at the cusp region; thereafter, Z started to respond from 77°N downward, and finally, Y started to respond from the south of 71°N. Thus, the geomagnetic crochet feature's appearance at the cusp region was only visible in the X component. It was not apparent in the Y and Z components at the cusp region. In the Z component, it appeared at stations below the 77°N, and in the Y component, it was visible at stations located below the 71°N. This is supported by the results of Viljanen and Tanskanen ([2013](#)), who examined 1-min averaged X, Y, and Z components of geomagnetic fields recorded from 13 northern high-latitude and nine southern high-latitude magnetometer stations. Their analysis showed that the X, Y, and Z components increase from subauroral latitudes (50°) to the auroral region (70°), most prominently in X and Z. The Y component depends largely on the sine of geomagnetic longitude because of the tilt of the geomagnetic coordinate system with respect to the geographic coordinate system in which X and Y are measured. The rotation of the X and Y components into this geomagnetic coordinate system reduced the azimuthal component to zero in most cases, confirming the tilted axisymmetric nature of the disturbance field (Stewart & Whaler, [1992](#)). Stening ([1977](#)) showed that the field-aligned currents substantially contribute to the Y component at low latitudes. Thus, the present result regarding the absence of the crochet feature in the Y component at the cusp region is consistent with the observations of Viljanen and Tanskanen ([2013](#)); Stewart and Whaler ([1992](#)); Belakhovsky et al. ([2019](#)).

4.2. Different Sensitivities and Profiles of Geomagnetic Activity

Among the three components, relatively small disturbances are observed in the Z component because the conducting Earth tends to shield vertical magnetic disturbances imposed by magnetospheric currents for example, (Yamazaki & Maute, [2017](#)). The Z component is affected by the local conductivity anomalies in the ground, and thus when a given station is located above a highly conducting structure, the vertical field variations tend to be smaller than in the surroundings (Taat et al., [2019](#); Viljanen & Tanskanen, [2013](#)). Further among the three components, an explicit appearance of a positive or negative spike in the northward component(X) at the Svalbard region (74°–80°N) and eastward component(Y) at lower latitudes (50°–71°N) is observed during the peak time of X1.5 flare. The positive/negative spike is sustained for 15–30 min. The positive spike in the X component appeared during flare peak time at Svalbard stations had an amplitude in range of 8–40 nT. For the lower latitudes (<70°N), the X component shows quick increase at flare peak time. The X component enhancements exhibit multiple peaks that become smoother and the duration of the enhancement prolongs as one descends in latitude. Thus, the crochet feature in the Svalbard region exhibits a sharp and short-lived positive spike in the X component, whereas, at lower latitudes, it exhibits broader maximum for 1–2 hr duration after the flare peak time. The variation of Y component at stations in latitudinal belt (50°–71°N) showed post-spike enhancement accompanied by multiple peaks at poleward high-latitude stations and smooth variation at equatorward mid-high-latitude stations. It is evident from comparing the variations of the Y component at stations (SOR to PEL) located >65°N latitude and stations (NUR to PPN) located <60°N latitude that the long-duration Y component enhancement is only seen in a small latitudinal belt and diminishes toward higher latitudes. The flare induced variation in Y component in the Svalbard region may have been obscured by irregular variations in the geomagnetic field (e.g., Grodji et al., [2022](#)) as explained above in Section [4.1](#). Furthermore, compared to higher latitude stations (Figure [5](#)), accompanying up and down fluctuations become smoother with lower latitudes (Figure [6](#)). The variation of the Z component only shows positive or negative spikes during the flare peak time, and their amplitude (~5 nT) is much smaller than it is for the Y component (~10 nT) at all stations. Thus, in general, present observations showed geomagnetic crochet of amplitude ~5–40 nT, and duration ~10–15 min during the peak time of X.5 flare, and their amplitude decreases toward lower latitudes. The observed crochet feature in the Svalbard region (stations NAL, LYR, and HOR) is identified as cusp crochet. Yamauchi et al. ([2020](#)) did not observe such type of geomagnetic crochet at cusp region (stations LYB and HOP in their case). At mid-high latitudes, the profile of geomagnetic crochet observed in present case seem similar to that of Yamauchi et al. ([2020](#)), yet amplitude of

crochet at flare peak time and post-spike enhancement in the present case (∼10 nT) is observed to be smaller from the that of Yamauchi et al. (2020) (amplitude; 70–200 nT).

An asymmetric response of different components and variance in their crochet shapes has been studied by Curto (2020). They found that the solar flare effect may not necessary appear in all the components of the geomagnetic field. Also, the shape of crochet is not predetermined and may vary from event to event or may differ in all three components. The reason for the appearance of crochet, particularly its shape, is due to the irregular temporal variations of solar disturbances and different relaxation times (Curto et al., 2016). Additionally, sfes are the result of the interaction between several radiation bands (X and UV) that appear at various altitudes of the sun, so they may or may not be synchronic and may have different relaxation times (Richmond & Venkateswaran, 1971). This fact can be visualized from the time evolution of the different EUV bands shown in Figure 2 wherein the relaxation times for 25.4, 28.4, 28/29 nm, and 30/31 nm EUV bands were determined to be about 31.2, 73.2, 24, and 50 min, respectively. Regarding this, Pandey et al. (2023) recently reported on flare energy emitted from various EUV bands and the delay between the impulsive phase (where the EUV peak occurs before the X-ray peak) and the thermal phase (where the EUV peak occurs after the X-ray peak). Their results showed a time difference between the two phases in the range of 0–25 min. In the case of X-class flares, the maximum time difference observed is about 7 min. The impulsive phase is connected with flare footpoints, whereas thermal emissions are more likely to involve the loop structure extending to the corona (Benz, 2017). The Sfe current closely follows the EUV flux variation, thus strongly indicating direct EUV modulation of the Sfe current as its cause. The greater EUV may alter electric fields and impact the overall current intensity (Owolabi et al., 2020).

4.3. Strength of Geomagnetic Crochet

The magnetometer observations revealed the presence of geomagnetic crochet of reduced amplitude (3–40 nT) in all three components. The small amplitude of the magnetic disturbance may be related to the location of an X1.5 solar flare at the solar limb (24°N, 88°W) and its intensity as compared to X9.3 flare reported by Yamauchi et al. (2020). Because of its limb position (N24W88), we expect a smaller X-ray flux as compared to what one would have been on the disk center albeit the role of other factors like solar zenith angle, seasons, solar cycle, latitudinal position of the observation station, flare intensity, and the active region's ability to produce successive flares (Grodji et al., 2022). However, its geomagnetic effects were still very significant. The greater magnitude of geomagnetic disturbances during the flare of 6 September 2017, as reported by Yamauchi et al. (2020) may be because of the location of larger X9.3 flare on the solar disk which is most likely to be observed over longer timescales. The transport paths of the irradiance/radiating particles from the acceleration site to the emission site must be different for the limb (3 July 2021) and disk flare (6 September 2017) because of location of the respective flares. For limb flares, irradiance and radiating particles accelerated to large optical distances than disk flares and thus, the thermosphere-ionosphere (TI) responds differently to limb and disk flares (Qian et al., 2019; Zhang et al., 2002). This fact is also supported by the results of Grodji et al. (2022) and Le et al. (2013). However, the extreme position of the flare would affect EUV radiation more than the X-ray radiation. The position of the flare on the sun's surface is not very relevant to their efficiency in producing geomagnetic effects, although there is a slightly better efficiency in producing geomagnetic effects for the disk flare compared to the limb flare (Curto & Gaya-Piquã, 2009). Thus the ionospheric response to solar flare above 150 km (where EUV dominates) is more affected by disk flares than limb flares. An independent and intended study is needed to evaluate the effect of an AR location on sfe, which is outside the scope of current work. Also, the intensity of the X class in the present case (i.e., X1.5) is comparatively lower than the X9.3 flare of 6 September 2017. Further the sfe on the TI system depends upon their characteristics, including flare rise and decay times for example, (Qian et al., 2011). Comparison of the two flares (X1.5 on 3 July 2021, and X9.3 on 6 September 2017) reveals that the X1.5 flare's irradiance reached the pre-flare flux level ∼30 min after the peak, whereas the X9.3 flare took ∼4 hr to reach the normal diurnal level. The TI effect further generates additional currents in the ionosphere, and their signatures appear as geomagnetic crochet, otherwise referred to the sfe.
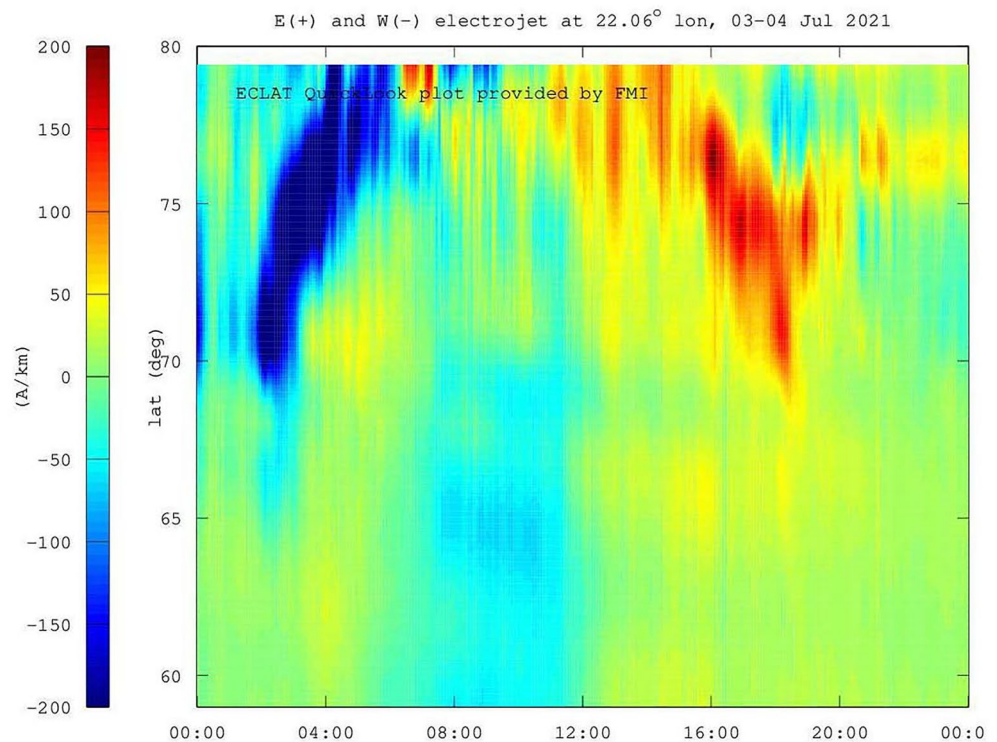
Figure 8. The pattern of the ionospheric equivalent current (IEC) system (including preexisting Sq current) on 3 July 2021 over an Atlantic Region is shown.

4.4. Latitudinal Profile of Amplitude and Phase of the Crochet

The X component shows a positive spike at the cusp region, the Y component shows a negative spike, and the Z component shows a positive spike in latitudes above 70°N and a negative spike in latitudes down to 70°N. Also the strength of the geomagnetic crochet decreased from poleward to equatorward stations. This is consistent with the variation of the auroral electrojets during periods of geomagnetic disturbance. For this, we have first checked geomagnetic field variation in all three components at different stations located from 10° to 25° E along nearly same latitude (not shown here). Observations show that the pattern (shape and phase) and amplitude remained nearly same longitudinally in belt of 10°–25°E. Thus, the shape of crochet (pattern, phase, and magnitude) may be associated with the latitudinal distribution of electric conductivity, or, in a broad manner, the local electrodynamics play an important role. As the configuration of geomagnetic field lines is different at the cusp region, auroral oval region, and mid-latitude, the resulting distribution of flare-induced IEC may have a different pattern at different latitudes. This could be well understood from the pattern of IEC which is discussed hereafter.

The observed latitudinal variation of crochet strength, shape, and time evolution is related to the latitudinal distribution and time evolution of the Ionospheric Equivalent Current (IEC). The IECs are a convenient means to study the characteristics of the currents in the ionosphere. These currents are directly connected to the field-aligned magnetospheric currents through ionosphere-magnetosphere coupling (Kamide & Baumjohann, 1993). The IEC represents only the divergence-free part of the actual ionospheric current, possibly apart from a relatively small and smooth north/south-directed background current. The pattern of equivalent ionospheric current (IEC) systems (including preexisting Sq current) on 3 July 2021, over the Atlantic Region, is shown in Figure 8.

The abscissa of Figure 8 shows the time in UT, and the left ordinate shows the geographic latitude. The color scale on the left gives the current density amplitude in A/km. At 100 km altitude, the IEC is calculated from the ground magnetometer and flows within the ionospheric plane. The red and blue patches in the contour show the strength of the eastward and westward currents, respectively. The IEC plot gives the diur-

nal development of the east and west auroral electrojets in the ionosphere. The current density (J) rapidly increased after the X1.5 solar flare at 14:18 UT in the latitudinal band of 65°–80°N and intensified at 14:30 UT centered on 78°N latitude, as shown in Figure 8. The level of eastward current on the other hand, began right at the start of the M2.7 solar flare at 07:04 UT. It can also be seen that the eastward current expanded rapidly toward lower latitudes with decrease in magnitude during the post-peak hours of the solar flare. Since the electron density increase means an increased ion-neutral density ratio, the ionospheric current is also expected to flow at lower altitudes where the tidal (Sq0) ion convection is more vigorous. Such changes can significantly enhance the preexisting ionospheric Sq0 current (Yamauchi et al., 2020). During the solar flare event of 24 September 2011 (Gopika et al., 2021), reported an increase in net eastward current at the equator of 1636% around 90 km and 200% around 105 km. In the present case, it is revealed from Figure 8 that the IEC increased by 200% around 65°N and ~300% around 75°N at ~22°E longitude sector. These results are consistent with the observations of Yamauchi et al. (2020), wherein they reported a sudden appearance in the IEC during the X9.3 flare of 6 September 2017. For the September 2017 event, the enhancement was westward below 70° geographic latitude and eastward at higher latitudes ~20°E and ~50°W longitude sectors. They reported that the enhanced level of westward and eastward currents was related to the sub-solar and high-latitudes of the northern hemisphere, respectively. Based upon the theory of electromagnetic induction, Nagata (1952) reported the geomagnetic effect of solar flares due to the sudden increase in ionospheric conductivity during the flare. The enhanced conductivity in the D-region or at the boundary between the D and E-regions of the ionosphere during a flare is believed to cause the sfes or crochet signatures (Pintér, 1967). A careful look at Figure 8 reveals that the strength of the eastward electrojet was strongest around 78°N (Svalbard region) at flare peak time and then decreased toward lower latitudes with the time. Thus, the time evolution of the latitudinal distribution of lower ionospheric conductivity can be interpreted as the time evolution of the strength and characteristics of geomagnetic disturbances. The decrease in the magnitude of the X and Z component's spike and the time sequence in the appearance of magnetic crochet (Z component, Figure 3) may be related to the time sequence of IEC as shown in Figure 8.

Like the amplitude, as discussed above, the phase of the crochet also depends upon the latitudinal distribution of IEC. Curto et al. (1994) showed that the phase change (positive or negative spikes) in the crochet signature appears as a physical consequence of the ionospheric current system geometry and is due to the displacement that the sfe system undergoes in longitude and/or latitude for the Sq current system. Furthermore, spikes and peaks in X and Z geomagnetic components are not observed synchronously (within a few seconds) in stations separated even by a few degrees of longitude. For example, the positive peak in the Z component appeared earlier at LYR, HOR, and HOP compared to BJN. The IEC current vectors are shown in Figure 9 wherein the magnetometer stations from which data are used in the calculation are shown as black-filled circles. Figure 9 shows the 2D vector directions corresponding to the peak of crochet (14:30 UT). It can be seen from the Figure 9 that the pattern of eastward currents is changing as one goes toward lower latitudes. In the region around the auroral oval or below the station's BJN (74°N, 19.2°E), a clear change in the directions of current vectors is seen. Above 70°N, the current vectors are in a clockwise direction, whereas at latitudes 65°N, the current vectors are set in an anticlockwise direction. A careful look on Figure 9 suggests that the current vectors close differently across 70°N (see around stations MAS and SOR). In contrast, if we look carefully the vectors around PEL and NUR stations, those are differently directed and also much subdued around NUR compared to PEL. Therefore, the magnetic variations across latitudes (for a given longitude) seem to be consistent with the variations in the equivalent current. This is the region between the upward Region 1 field-aligned current and the downward Region 2 field-aligned current (Yamauchi & Slapak, 2018). Thus, the Figure 9 clearly demonstrates a two-cell current system during the X1.5 flare. At mid-high latitude stations, the current vectors are hardly noticeable. This is the reason why very weak crochet is observed at lower latitudes. In this regard Belakhovsky et al. (2019), also observed that the equivalent ionospheric currents at the high-latitude end of the profile suddenly changed their direction from predominantly east-west (E-W) to north-south (N-S) in the geomagnetic impulsive disturbance of the substorm event of 17 March 2013. Since the multiple current systems simultaneously contribute to high-latitude conductivity during solar flares, the pattern of geomagnetic field variation at different stations may differ according to equivalent current vectors. However, it is impossible to identify a particular electric current contributor responsible for a particular crochet pattern at different stations.
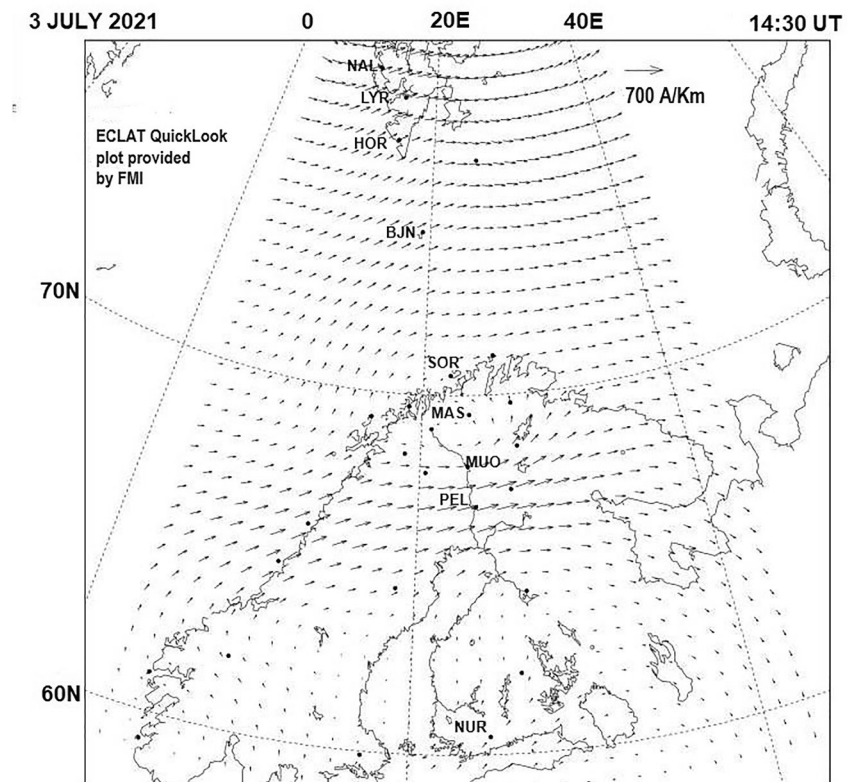
Figure 9. The ionospheric equivalent current (IEC) distribution at 14:30 UT on 3 July 2021 over magnetometer stations chosen in the present case is shown.

5. Conclusion

Using IMAGE and Intermagnet magnetometers network data, we investigated the geomagnetic signatures of X1.5 solar flare at the limb (24°N, 88°W) that occurred on 3 July 2021, in the newly emerged NOAA AR12838. The temporal variation in X-rays and EUV reveals that the X1.5 flare appeared at ~14:18 UT, peaked at ~14:29 UT, and decayed at ~14:34 UT. The variation in X-ray intensity showed that it quickly (<30 min) resettled to a quiet level. The important results derived from this study are summarized as follows:

1. The X1.5 flare occurred in a unique solar active region which initially appeared as a bi-polar intense magnetic region on the west limb, later identified as beta-type AR. However, it was identified as a pores region in HMI continuum images within hours of its appearance. AR12838 produced X1.5 solar flare at 14:18 UT on 3 July 2021; the next day, it rotated behind the west limb.
2. The geomagnetic crochet features observed during solar flare event of 3 July 2021 are observed to have the following characteristics: (a) an enhancement in geomagnetic field components during flare peak time without a spike; (b) a positive or negative spike in geomagnetic field components, particularly an explicit and coherence appearance in the Y component at high-latitude stations (50°N, 70°N); and (c) a post-spike increase in geomagnetic field components accompanied by multiple peaks at poleward stations and smoothed variation at mid-high latitude stations.
3. The important finding of the present study is the observation of geomagnetic crochet in the polar cusp region (~78°N) with a smaller magnitude (8–40 nT) and a shorter duration (10–15 min). Also, our observations showed geomagnetic crochet features during peak time of X1.5 flare followed by enhanced level of geomagnetic field components at mid-high latitudes of amplitude; 5–10 nT. The observations of geomagnetic crochet features at cusp region and at mid-high latitudes is observed to be diminished in magnitude compared to those reported by Yamauchi et al. (2020) for a much intense flare of X9.3 class.
4. The time evolution of the geomagnetic crochet and its latitudinal variation is observed to be coherent with the time evolution of the latitudinal distribution of ionospheric equivalent current.

Data Availability Statement

The XRS-A/B, EUV irradiance, geomagnetic field components (IMAGE and INTERMAGNET magnetometer data), and geomagnetic parameters (ASY, SYM, and PCN) are published with Mendeley Data (https://doi.org/10.17632/g4jsfkfh69.1). These data can be obtained using the link: https://data.mendeley.com/datasets/g4jsfkfh69/1. The two-dimensional data of equivalent ionospheric current (IEC) vectors in a latitude-longitude grid are obtained using the instant-run interface at https://space.fmi.fi/MIRACLE. To obtain IEC plot, users need to fill the event inputs in form https://space.fmi.fi/MIRACLE/iono_2D.php#form.Similarly the 2D equivalent current vectors could be obtained from image magnetometer website by filing event selection form https://space.fmi.fi/MIRA-CLE/iono_2D.php#form.

References

Barta, V., Sátori, G., Berényi, K. A., Kis, A., & Williams, E. (2019). Effects of solar flares on the ionosphere as shown by the dynamics of ionograms recorded in Europe and South Africa. *Annales Geophysicae*, *37*(4), 747–761. https://doi.org/10.5194/angeo-37-747-2019

Belakhovsky, V., Pilipenko, V., Engebretson, M., Sakharov, Y., & Selivanov, V. (2019). Impulsive disturbances of the geomagnetic field as a cause of induced currents of electric power lines. *Journal of Space Weather and Space Climate*, *9*, A18. https://doi.org/10.1051/swsc/2019015

Benz, A. O. (2017). Flare observations. *Living Reviews in Solar Physics*, *14*(1), 2. https://doi.org/10.1007/s41116-016-0004-3

Chulliat, A., Vigneron, P., & Hulot, G. (2016). First results from the Swarm dedicated ionospheric field inversion chain. *Earth Planets and Space*, *68*(1), 104. https://doi.org/10.1186/s40623-016-0481-6

Curto, J., Amory-Mazaudier, C., Torta, J., & Menvielle, M. (1994). Solar flare effects at ebre: Regular and reversed solar flare effects, statistical analysis (1953 to 1985), a global case study and a model of elliptical ionospheric currents. *Journal of Geophysical Research*, *99*(3), 3945–3954. https://doi.org/10.1029/93JA02270

Curto, J. J. (2020). Geomagnetic solar flare effects: A review. *Journal of Space Weather and Space Climate*, *10*, 27. https://doi.org/10.1051/swsc/2020027

Curto, J. J., Castell, J., & Del Moral, F. (2016). Sfe: Waiting for the big one. *Journal of Space Weather and Space Climate*, *6*, A23. https://doi.org/10.1051/swsc/2016018

Curto, J. J., & Gaya-Piquã©, L. R. (2009). Geoeffectiveness of solar flares in magnetic crochet (sfe) production: Iiâ€"dependence on the detection method. *Journal of Atmospheric and Solar-Terrestrial Physics*, *71*(17), 1705–1710. https://doi.org/10.1016/j.jastp.2007.12.003

Dellinger, J. H. (1937). Sudden ionospheric disturbances. *Terrestrial Magnetism and Atmospheric Electricity*, *42*(1), 49–53. https://doi.org/10.1029/TE042i001p00049

Dmitriev, A., & Yeh, H.-C. (2008). Geomagnetic signatures of sudden ionospheric disturbances during extreme solar radiation events. *Journal of Atmospheric and Solar-Terrestrial Physics*, *70*(15), 1971–1984. https://doi.org/10.1016/j.jastp.2008.05.008

Dodson, H. W., & Hedeman, E. R. (1958). Crochet-associated flares. *Apj*, *128*, 636. https://doi.org/10.1086/146577

Fröhlich, C. (2009). Evidence of a long-term trend in total solar irradiance. *Astronomy and Astrophysics*, *501*(3), L27–L30. https://doi.org/10.1051/0004-6361/200912318

Gopika, P. G., Ambili, K. M., & Choudhary, R. K. (2021). The response of the d and e regions of the equatorial ionosphere to solar flare events. *Journal of Geophysical Research: Space Physics*, *126*(12), e2021JA029350. https://doi.org/10.1029/2021JA029350

Grodji, O. D. F., Doumbia, V., Amaechi, P. O., Amory-Mazaudier, C., Nâ€guessan, K., Diaby, K. A. A., et al. (2022). A study of solar flare effects on the geomagnetic field components during solar cycles 23 and 24. *Atmosphere*, *13*(1), 69. https://doi.org/10.3390/atmos13010069

Kamide, Y., & Baumjohann, W. (1993). Magnetosphere-ionosphere coupling physics chemistry in space (Vol. *23*).

Le, H., Liu, L., Chen, Y., & Wan, W. (2013). Statistical analysis of ionospheric responses to solar flares in the solar cycle 23. *Journal of Geophysical Research: Space Physics*, *118*(1), 576–582. https://doi.org/10.1029/2012JA017934

Nagata, T. (1952). Characteristics of the solar flare effect (Sqa) on geomagnetic field at Huancayo (Peru) and at kakioka (Japan). *Journal of Geophysical Research*, *57*(1), 1–14. https://doi.org/10.1029/JZ057i001p00001

Newell, P. T., & Meng, C.-I. (1988). The cusp and the cleft/boundary layer: Low-altitude identification and statistical local time variation. *Journal of Geophysical Research*, *93*(A12), 14549–14556. https://doi.org/10.1029/JA093iA12p14549

Nishida, A. (1968). Coherence of geomagnetic DP 2 fluctuations with interplanetary magnetic variations. *Journal of Geophysical Research*, *73*(17), 5549–5559. https://doi.org/10.1029/JA073i017p05549

Owolabi, C., Lei, J., Bolaji, O. S., Ren, D., & Yoshikawa, A. (2020). Ionospheric current variations induced by the solar flares of 6 and 10 September 2017. *Space Weather*, *18*(11), e2020SW002608. https://doi.org/10.1029/2020SW002608

Pandey, K., Chakrabarty, D., Kumar, A., Bhardwaj, A., Biswal, S., Hussey, G., & Yadav, A. (2023). Characteristics of x-class flares of solar cycles 23 and 24 in x-ray and euv bands. *Advances in Space Research*, *71*(12), 5438–5452. https://doi.org/10.1016/j.asr.2023.02.022

Pintér, Š. (1967). Geomagnetic crochets of solar flares observed in Hurbanovo. *Bulletin of the Astronomical Institutes of Czechoslovakia*, *18*, 274.

Prikryl, P., Spogli, L., Jayachandran, P. T., Kinrade, J., Mitchell, C. N., Ning, B., et al. (2011). Interhemispheric comparison of gps phase scintillation at high latitudes during the magnetic-cloud-induced geomagnetic storm of 5â€"7 april 2010. *Annales Geophysicae*, *29*(12), 2287–2304. https://doi.org/10.5194/angeo-29-2287-2011

Pudovkin, M. I. (1974). Electric fields and currents in the ionosphere. *Space Science Reviews*, *16*(5–6), 727–770. https://doi.org/10.1007/bf00182599

Qian, L., Burns, A. G., Chamberlin, P. C., & Solomon, S. C. (2010). Flare location on the solar disk: Modeling the thermosphere and ionosphere response. *Journal of Geophysical Research*, *115*(A9), A09311. https://doi.org/10.1029/2009JA015225

Qian, L., Burns, A. G., Chamberlin, P. C., & Solomon, S. C. (2011). Variability of thermosphere and ionosphere responses to solar flares. *Journal of Geophysical Research*, *116*(A10), A10309. https://doi.org/10.1029/2011JA016777

Qian, L., Wang, W., Burns, A. G., Chamberlin, P. C., Coster, A., Zhang, S.-R., & Solomon, S. C. (2019). Solar flare and geomagnetic storm effects on the thermosphere and ionosphere during 6â€"11 september 2017. *Journal of Geophysical Research: Space Physics*, *124*(3), 2298–2311. https://doi.org/10.1029/2018JA026175

Rao, S. S., & Chakraborty, M. (2022). Ionospheric disturbances during x1.5 class solar flare of 3 July 2021. In *2022 ursi regional conference on radio science (USRI-RCRS)* (pp. 1–4). https://doi.org/10.23919/URSI-RCRS56822.2022.10118497

Rastogi, R., Kaushika, N., & Trivedi, N. (1965). Solar flare crochet and sudden commencement in h within the equatorial electrojet region. *Journal of Atmospheric and Terrestrial Physics*, *27*(5), 663–668. https://doi.org/10.1016/0021-9169(65)90135-2

Rastogi, R. G., Chandra, H., & Yumoto, K. (2013). Unique examples of solar flare effects in geomagnetic H field during partial counter electrojet along CPMN longitude sector. *Earth Planets and Space*, *65*(9), 1027–1040. https://doi.org/10.5047/eps.2013.04.004

Rastogi, R. G., Pathan, B. M., Rao, D. R. K., Sastry, T. S., & Sastri, J. H. (1999). Solar flare effects on the geomagnetic elements during normal and counter electrojet periods. *Earth Planets and Space*, *51*(9), 947–957. https://doi.org/10.1186/BF03351565

Richmond, A. D., & Maute, A. (2014). Ionospheric electrodynamics modeling. In *Modeling the ionosphere–thermosphere system* (pp. 57–71). American Geophysical Union (AGU). https://doi.org/10.1002/9781118704417.ch6

Richmond, A. D., & Venkateswaran, S. V. (1971). Geomagnetic crochets and associated ionospheric current systems. *Radio Science*, *6*(2), 139–164. https://doi.org/10.1029/RS006i002p00139

Russell, C. (2000). The polar cusp. *Advances in Space Research*, *25*(7), 1413–1424. https://doi.org/10.1016/S0273-1177(99)00653-5

Sahai, Y., Becker-Guedes, F., Fagundes, P. R., Lima, W. L. C., de Abreu, A. J., Guarnieri, F. L., et al. (2007). Unusual ionospheric effects observed during the intense 28 October 2003 solar flare in the Brazilian sector. *Annales Geophysicae*, *25*(12), 2497–2502. https://doi.org/10.5194/angeo-25-2497-2007

Sammis, I., Tang, F., & Zirin, H. (2000). The dependence of large flare occurrence on the magnetic structure of sunspots. *The Astrophysical Journal*, *540*(1), 583–587. https://doi.org/10.1086/309303

Schwenn, R. (2006). Space weather: The solar perspective. *Living Reviews in Solar Physics*, *3*(1), 2. https://doi.org/10.12942/lrsp-2006-2

Stening, R. J. (1977). Field-aligned currents driven by the ionospheric dynamo. *Journal of Atmospheric and Terrestrial Physics*, *39*(8), 933–937. https://doi.org/10.1016/0021-9169(77)90175-1

Stewart, D. N., & Whaler, K. A. (1992). Geomagnetic disturbance fields: An analysis of observatory monthly means. *Geophysical Journal International*, *108*(1), 215–223. https://doi.org/10.1111/j.1365-246X.1992.tb00851.x

Taat, A., Abbas, M., & Jusoh, M. H. (2019). The response of geomagnetic h and z components during x-class solar flare. *Journal of Physics: Conference Series*, *1152*(1), 012031. https://doi.org/10.1088/1742-6596/1152/1/012031

Thome, G. D., & Wagner, L. S. (1971). Electron density enhancements in the e and f regions of the ionosphere during solar flares. *Journal of Geophysical Research*, *76*(28), 6883–6895. https://doi.org/10.1029/JA076i028p06883

Tsurutani, B. T., Shibata, K., Akasofu, S.-I., & Oka, M. (2009). A two-step scenario for both solar flares and magnetospheric substorms: Short duration energy storage. *Earth Planets and Space*, *61*(5), 555–559. https://doi.org/10.1186/BF03352921

Viljanen, A. (1997). The relation between geomagnetic variations and their time derivatives and implications for estimation of induction risks. *Geophysical Research Letters*, *24*(6), 631–634. https://doi.org/10.1029/97GL00538

Viljanen, A., & Tanskanen, E. (2013). High-latitude magnetic fields and their time derivatives: Interhemispheric similarities. *Earth Planets and Space*, *65*(1), 45–49. https://doi.org/10.5047/eps.2012.05.014

Watari, S. (2022). Extremely large flares/multiple large flares expected from sunspot groups with large area. *Earth Planets and Space*, *74*(1), 115. https://doi.org/10.1186/s40623-022-01676-5

Willis, D. M. (1969). The influx of charged particles at the magnetic cusps on the boundary of the magnetosphere. *Planetary and Space Science*, *17*(3), 339–348. https://doi.org/10.1016/0032-0633(69)90067-1

Yamauchi, M., Johnsen, M. G., Enell, C.-F., Tjulin, A., Willer, A., & Sormakov, D. A. (2020). High-latitude crochet: Solar-flare-induced magnetic disturbance independent from low-latitude crochet. *Annales Geophysicae*, *38*(6), 1159–1170. https://doi.org/10.5194/angeo-38-1159-2020

Yamauchi, M., & Slapak, R. (2018). Cusp current system. In *Electric currents in geospace and beyond* (pp. 339–358). American Geophysical Union (AGU). https://doi.org/10.1002/9781119324522.ch20

Yamazaki, Y., & Maute, A. (2017). Sq and EEJ—A review on the daily variation of the geomagnetic field caused by ionospheric dynamo currents. *Space Science Reviews*, *206*(1–4), 299–405. https://doi.org/10.1007/s11214-016-0282-z

Zhang, D. H., Xiao, Z., Igarashi, K., & Ma, G. Y. (2002). Gps-derived ionospheric total electron content response to a solar flare that occurred on 14 July 2000. *Radio Science*, *37*(5), 1–11. https://doi.org/10.1029/2001RS002542